Volume 2, Number 2 (June 2006) p. 187-227 ISSN 1809-1121
Revista IBRACON de Estruturas
IBRACON Structural Journal

Finite Element Model for Segmental Structures

Modelo de Elementos Finitos para o Estudo de Estruturas Segmentadas



ALINE DA SILVA RIBEIRO[a]
aribeiro@ppgec.ufrgs.br

AMÉRICO CAMPOS FILHO[b]
americo@ufrgs.br

ALEXANDRE RODRIGUES PACHECO[c]
apacheco@ufrgs.br

Abstract

When bridge construction is considered, the application of externally post-tensioned segmental members is a very attractive solution, especially when compared to more classical construction methods. The use of this solution results in smaller precast elements tied together by post-tensioned tendons, upbringing such advantages as fast and versatile construction, high quality control and lower overall cost. In this paper, a formulation based on the Finite Element Method is discussed. This formulation is used to numerically simulate the structural behavior of members composed of externally post-tensioned segments. These analyses not only allow serviceability limit states verifications when sections are fully compressed, but also allow verifications of ultimate limit states when joint openings and load transfers at the joints are considered. Additionally, to evaluate the accuracy of the numerical results of the computational model a comparison to experimental data from the literature is performed.

Keywords: Finite Element Method, Segmental Construction, Bridges, External Prestressing.

Resumo

Aduelas protendidas externamente, utilizadas em pontes, contrastam com as clássicas construções monolíticas, consistindo de "pequenos" segmentos pré-moldados protendidos por cordoalhas externas. Há muitas vantagens na utilização deste tipo de composição, como rapidez e versatilidade na construção, alto controle de qualidade e economia. No presente trabalho, discute-se uma formulação, baseada no método dos elementos finitos, para simular o comportamento de estruturas compostas por aduelas externamente protendidas. Esta formulação permite tanto a análise de situações de serviço, onde as seções permanecem completamente comprimidas, como também de situações últimas, onde se considera a abertura das juntas e a transferência de esforços através das mesmas. Para verificar a adequação do modelo computacional, compararam-se resultados numéricos com valores experimentais disponíveis na literatura.

Palavras-chave: Elementos finitos, Construções segmentadas, Pontes, Protensão externa.

[a] *Universidade Federal do Rio Grande do Sul, PPGEC, aribeiro@ppgec.ufrgs.br, Av. Osvaldo Aranha, 99 - 3º andar, Porto Alegre, Brazil;*
[b] *Universidade Federal do Rio Grande do Sul, PPGEC, americo@ufrgs.br, Av. Osvaldo Aranha, 99 - 3º andar, Porto Alegre, Brazil;*
[c] *Universidade Federal do Rio Grande do Sul, PPGEC, apacheco@ufrgs.br, Av. Osvaldo Aranha, 99 - 3º andar, Porto Alegre, Brazil.*

1 Introduction

It is not unusual to have the main aspects of a bridge design defined after the choice of its construction method. The choice of construction method is based on numerous factors such as the span length, equipment availability, construction timetable, and economic aspects. The span-by-span method for prestressed bridge construction, as illustrated in figure 1, has been largely adopted in many countries.
The main advantages of the use of precast segments are the high quality control, the need for smaller construction sites, fast construction, and the flawless finishing due to the metal or concrete formwork.
Recently, a growing attention has been directed towards the external prestressing system. In this system, the cables are placed inside the precast segments, but they are in contact with the concrete only at the deviation blocks and anchorages. They are inside polyethylene sheaths and embedded in a layer of cement grout for protection against corrosion (figure 2).
The Bang Na Expressway Bridge [3] in Bangkok, Thailand, was built using this technique of externally prestressed

Figure 1 – Schematic of the positioning procedure of a precast segment (1)

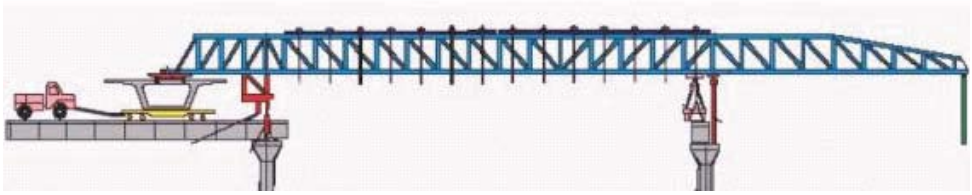

Figure 2 – Externally prestressed tendons (2)

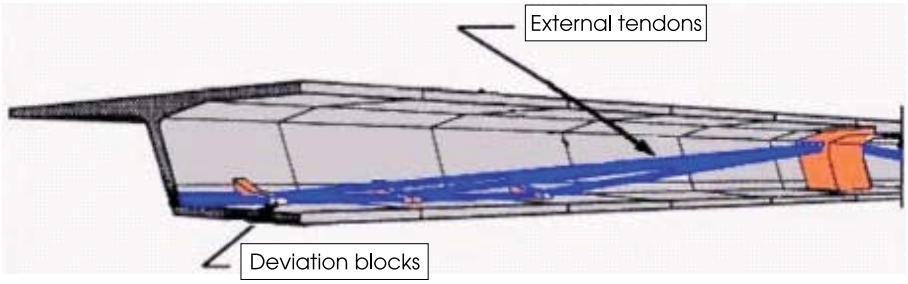

Figure 3 – (a) Bang Na Expressway bridge in Bangkok (b) Transportation of segments (3)

(a)

(b)

Figure 4 – Joint opening due to positive bending moment (2)

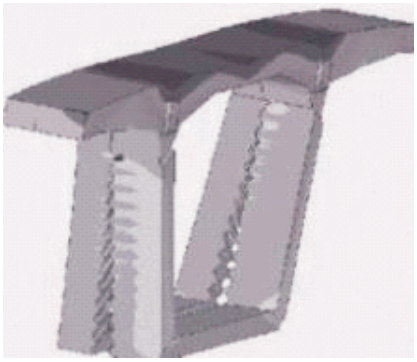

Figure 5 – Elasto-viscoplastic model

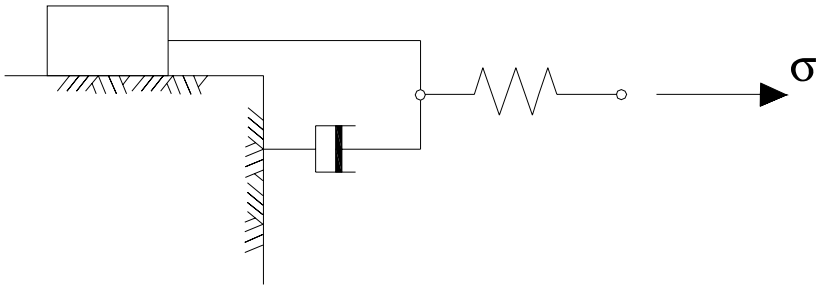

with dry joints. It is the longest in the world with its 55 km in total length (34 miles), and is the largest structure that has been built with precast segments (figure 3a). The construction technique allowed 1,800 segments to be manufactured per month. One of these segments, weighing 10 tons and measuring 27 m (89 ft) in length, is shown being transported in figure 3b.

The objective of this paper is to present a computational model based on the finite element method, and which was developed by Ribeiro [4], for the study of segmentally precast structures under plane stress state. The modeling of joints between segments of this type of structure with one-dimensional contact elements by Habraken and Cescotto [5] is particularly evaluated. Initially, a finite element model for nonlinear analysis of the concrete and the steel is presented. Later, a formulation for the contact elements that model the joints between the segments of the structure will be described.

Under service load, the structure is completely under compression and, consequently, its joints are closed. During ultimate conditions, the joints are opened because of tensile stresses (figure 4), which results in a stiffness reduction of the structure. The constitutive models used, the different prestressing systems implemented in the computational model, as well as comparisons between the numerical results with experimental ones gathered from the literature are also presented, Aparicio *et al*. [6].

2 Elasto-viscoplastic analysis by finite element modeling

The implemented model presents an incremental algorithm on loads by Owen and Hinton [7] for the solution of the elastoplastic part of the problem. An incremental algorithm in time, also by Owen and Hinton [7] same authors, is used for the viscoelastic part. The behavior of the materials is determined as a function of an elasto-viscoplastic model represented by one spring in series with one viscous dashpot and in parallel with one friction slider element, as shown in figure 5. With the use of this model, solution to elasto-plastic problems can be found when the structure reaches a steady state. On the other hand, solution to the viscoelastic problem, is achieved when the equivalent yield stress of the viscous dashpot is assigned to zero.

Figure 6 – The Overlay model used

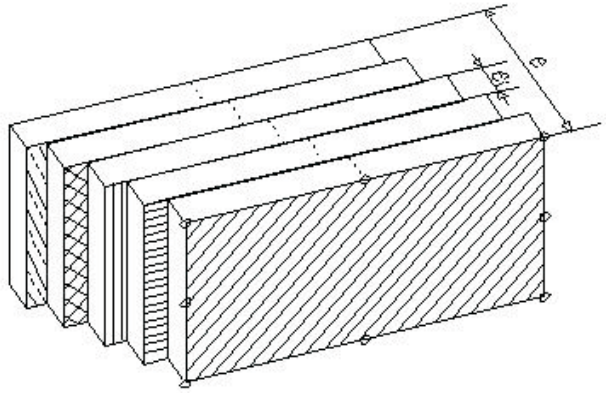

Figure 7 – Deformable Solids

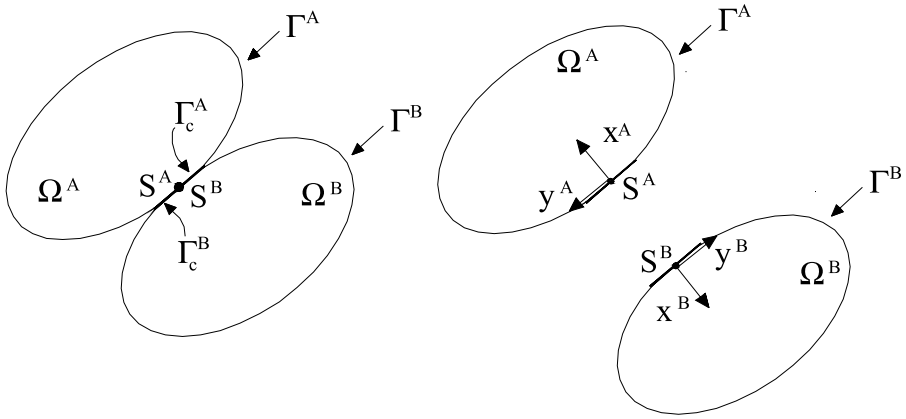

According to Pande *et al.* [8], the overlay model could be used when a response from a complex material such as concrete is desired, since it can simulate viscoelastic behavior with aging (figure 6). The material to be analyzed is divided into a convenient number of layers with distinct mechanical properties, and under the same total deformation. The total stress field is obtained by adding the contributions from each layer.
The rheological model is composed by a number of Maxwell elements in paralle. The model's parameters are the thicknesses of the layers, e_i, their moduli of elasticity, E_i, their dampening constants, γ_i, . A model with five layers was adopted.

3 Application of the finite element method

3.1 Finite Elements for the concrete

The concrete is represented by two-dimensional isoparametric elements of 4, 8, or 9 nodes [7]. A formulação dos elementos isoparamétricos quadráticos permite gerar elementos com lados curvos e modelar mais adequadamente os contornos irregulares de peças a serem analisadas. The elements present two degrees of freedom per node, corresponding to the translations in directions x and y of the global system of coordinates and ξ and η of the local normalized coordinates. Joints are represented by one-dimensional contact elements of 3 nodes, and are discussed in the next section. The nodes of each contact element match with the nodes of the concrete element to which it is associated.

3.2 Finite elements for the steel

The embedded reinforcement model is typically used in finite element analyses of structural concrete. The embedded reinforcement model proposed by Elwi and

Figure 8 – Contact elements

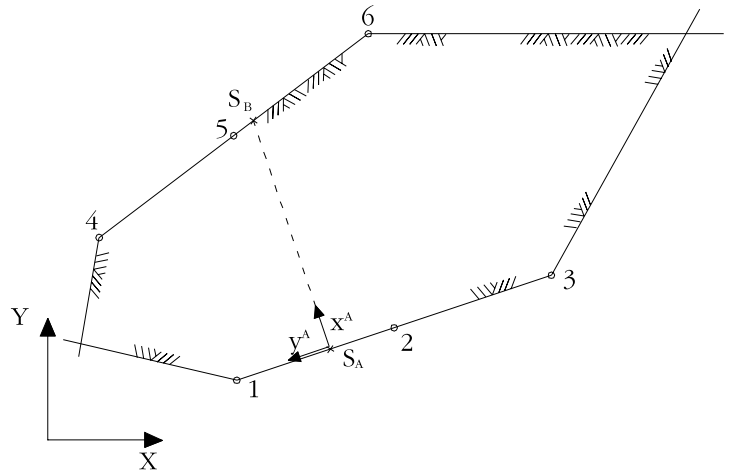

Figure 9 – Coordinates system for the contact elements

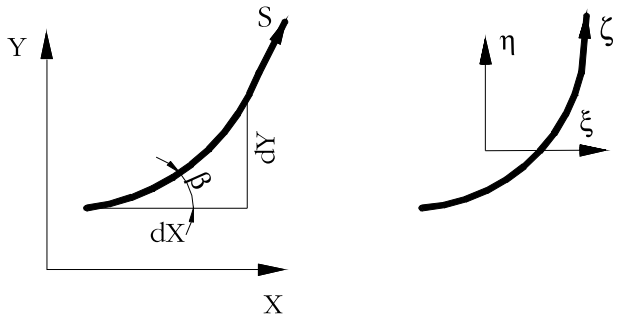

Hrudey [9] is used in this paper. The model considers the reinforcement subjected only to longitudinal axial loads and the displacements of any of its points equal to the concrete element in which it is embedded. Therefore, reinforcement bars only contribute to the longitudinal stiffness of concrete elements, allowing an arbitrary disposition of bars with no generation of new variables to the problem. When external prestressing cables are considered, they are assigned dummy elements that are considered parallel to the real elements of the structure.

4 Contact Elements

4.1 Formulation

The formulation used (Habraken and Cescotto [5]) considers two solids A and B with volumes Ω^A and Ω^B and perimeters Γ^A and Γ^B, respectively, as shown in figure 7. Both solids are in contact through the surfaces Γ_C^A and Γ_C^B. The coordinates of the local system are defined by the vector x, which is normal to the contact surface at point S (S^A or S^B), and by the vector y, which is tangent to the same surface, at the same point. It is considered that the nodes 1, 2 and 3 pertain to the contact element of the solid A and the nodes 4, 5 and 6 pertains to the contact element of the solid B, as shown in figure 8. The contact elements are described through their global coordinates (X,Y):

$$(X_j, Y_j) \quad j=1,2,3,4,5,6, \tag{1}$$

where j is the number of the node.

The local reference system (x^A, y^A) is given by:

$$\begin{aligned} x^A &= X\cos\beta + Y\sin\beta, \\ y^A &= -X\sin\beta + Y\cos\beta, \end{aligned} \tag{2}$$

In order to determine the co-sines of β, it is necessary to define a coordinate s and a differential element of length ds along the contact element (illustrated in figure 9). Thus:

$$\begin{aligned} \cos\beta &= \frac{dX}{ds} = \frac{dX}{d\zeta}\frac{d\zeta}{ds} \\ \sin\beta &= \frac{dY}{ds} = \frac{dY}{d\zeta}\frac{d\zeta}{ds} \end{aligned} \tag{3}$$

$$\frac{ds}{d\zeta} = \sqrt{\left(\frac{dX}{d\zeta}\right)^2 + \left(\frac{dY}{d\zeta}\right)^2}, \tag{4}$$

where:

$$\begin{Bmatrix} \frac{dX}{d\zeta} \\ \frac{dY}{d\zeta} \end{Bmatrix} = \sum_{j=1}^{n} \begin{bmatrix} \frac{dH_j}{d\zeta} & 0 \\ 0 & \frac{dH_j}{d\zeta} \end{bmatrix} \begin{Bmatrix} X_j \\ Y_j \end{Bmatrix}. \tag{5}$$

and n is the number of nodes of the contact element.
The one-dimensional interpolation function, H_j, are expressed in terms of a normalized coordinate, ζ, which limits are $-1 \le \zeta \le +1$, as shown in the next section. Thus, the global coordinates of a point located in the interior of an element are expressed in terms of interpolation functions, H_j, where j is the contact element number:

$$\begin{Bmatrix} X \\ Y \end{Bmatrix} = \sum_{j=1}^{n} \begin{bmatrix} H_j(\zeta) & 0 \\ 0 & H_j(\zeta) \end{bmatrix} \begin{Bmatrix} X_j \\ Y_j \end{Bmatrix}. \tag{6}$$

Therefore the global coordinates of S^A are:

$$\begin{aligned} X^A &= \left[\left(\frac{\zeta_A^{\,2} - \zeta_A}{2}\right)X_1 + \left(1 + \zeta_A^{\,2}\right)X_2 + \left(\frac{\zeta_A^{\,2} + \zeta_A}{2}\right)X_3\right], \\ Y^A &= \left[\left(\frac{\zeta_A^{\,2} - \zeta_A}{2}\right)Y_1 + \left(1 + \zeta_A^{\,2}\right)Y_2 + \left(\frac{\zeta_A^{\,2} + \zeta_A}{2}\right)Y_3\right], \end{aligned} \tag{7}$$

where ζ_A is the natural coordinate of S^A.
In order to determinate the opposite contact element, it is necessary to trace a line that passes through S^A and is directed toward x^A. The equation of this line is given by:

$$\begin{cases} X = X^A + \lambda\cos\beta \\ Y = Y^A + \lambda\sin\beta \end{cases} \tag{8}$$

where λ is the distance between S^A and the point where the line intercepts the opposite contact element.. Therefore the equation of the line is given by:

$$\begin{cases} X^B = X^A + \lambda\cos\beta \\ X^B = X^A + \lambda\sin\beta \end{cases} \tag{9}$$

where the global coordinates X^B and Y^B are given by:

$$\begin{aligned} X^B &= \left[\left(\frac{\zeta_B^{\,2} - \zeta_B}{2}\right)X_4 + \left(1 + \zeta_B^{\,2}\right)X_5 + \left(\frac{\zeta_B^{\,2} + \zeta_B}{2}\right)X_6\right], \\ Y^B &= \left[\left(\frac{\zeta_B^{\,2} - \zeta_B}{2}\right)Y_4 + \left(1 + \zeta_B^{\,2}\right)Y_5 + \left(\frac{\zeta_B^{\,2} + \zeta_B}{2}\right)Y_6\right]. \end{aligned} \tag{10}$$

where ζ_B is the natural coordinate of S^B.

Applying equation (10) in equation (9), the following equation is found:

$$\left[\left(\frac{\zeta_B^{\,2}-\zeta_B}{2}\right)X_4+\left(1+\zeta_B^{\,2}\right)X_5+\left(\frac{\zeta_B^{\,2}+\zeta_B}{2}\right)X_6\right]=X^A+\lambda\cos\beta$$
$$\left[\left(\frac{\zeta_B^{\,2}-\zeta_B}{2}\right)Y_4+\left(1+\zeta_B^{\,2}\right)Y_5+\left(\frac{\zeta_B^{\,2}+\zeta_B}{2}\right)Y_6\right]=Y^A+\lambda\sin\beta \qquad (11)$$

Solving the system, the values for ζ_B and λ can be found, where ζ_B is the location of S^B and λ is the distance between S^A and S^B (integration points of the contact elements).
The determination of λ at the element nodes is not readily done, since there is no explicit form for the inverse of equation 12. However, the inverse mapping can be done numerically through a non-linear system solution algorithm.

$$\lambda=\sum_{j=1}^{n}H_j\lambda_j,\quad j=1,2,3. \qquad (12)$$

Upon determining the distance λ to the points that define the geometry of the contact element being analyzed, a second phase is carried out where the opposed contact element is identified by ζ_B between -1 and +1. The third phase consists of the verification of whether the two bodies are together (λ ≥ 0), which adds terms to the stiffness matrix of the structure. With the increase of the distance between the bodies (λ < 0), these terms are removed and the nodes of the contact elements begin to have different displacements from those of opposed contact element.

4.2 Contact element shape functions

The interpolation functions for the contact elements are Lagrangian polynomials defined according to Zienkiewicz [10] as:

$$H^m(\zeta)=\prod_{\substack{i=1\\k\neq i}}^{n}\frac{(\zeta-\zeta_i)}{(\zeta_k-\zeta_i)} \qquad (13)$$

which is equal to 1 when $\zeta = \zeta_k$, and zero when $\zeta = \zeta_j$, where $i \neq k$.
For the three-node element, the following shape functions are found:

$$H_1(\zeta)=\frac{\zeta^2-\zeta}{2},$$
$$H_2(\zeta)=1-\zeta^2,$$
$$H_3(\zeta)=\frac{\zeta^2+\zeta}{2}. \qquad (14)$$

5 Constitutive models

5.1 Introduction

Non-linear behavior of materials should be considered for the analysis of reinforced and prestressed concrete structures. A typical structural concrete behavior is presented in figure 10. The sources of non-linearities are: concrete

Figure 10 – Typical load versus deflection diagram for reinforced concrete elements

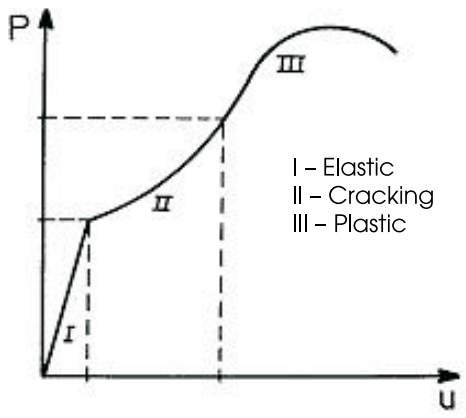

cracking; concrete and steel plastification; differences in tensile and compressive strengths of concrete; nonlinear stress-strain relationship and time-related phenomena such as concrete creep and shrinkage and prestressing steel relaxation. Other factors also include aggregate interlock and the dowel effect. Through the finite element analysis, one can carry out a more systematic approach to these phenomena and analyze each integration point in both concrete and steel elements.

5.2 Constitutive models for the concrete in compression

A hardening elasto-plastic model was used for concrete in compression. The model is composed of a failure criterion, a yielding criterion, and a hardening rule. For the uncracked concrete, an isotropic behavior was admitted. Its failure surface can be expressed as:

$$f(I_1, J_2, J_3) = 0, \tag{15}$$

where I_1 is the first invariant of the stress tensor, and J_2 and J_3 are the second and the third invariants of the deviatoric stress tensor. In this paper, the failure criterion proposed by Ottosen [11] and that is also adopted by the CEB-FIP Model Code 1990 [12] was assumed, and is given as:

$$\alpha \frac{J_2}{f_{cm}^2} + \lambda \frac{\sqrt{J_2}}{f_{cm}} + \beta \frac{I_1}{f_{cm}} - 1 = 0, \tag{16}$$

where f_{cm} is the mean compressive strength of concrete and:

$$\begin{cases} \lambda = c_1 \cos[1/3 \arccos(-c_2 \sin 3\theta)], \text{para} \sin 3\theta \le 0 \\ \lambda = c_1 \cos[\pi/3 - 1/3 \arccos(c_2 \sin 3\theta)], \text{para} \sin 3\theta > 0 \end{cases} \tag{17}$$

The four parameters of the model, α, β, c_1 and c_2 are determined according to the CEB-FIP Model Code 1990 [12] from the relation between the mean uniaxial compressive strength, f_{cm}, and the mean uniaxial tensile strength, f_{tm}, of the concrete, which is given as:

$$k = \frac{f_{tm}}{f_{cm}}, \tag{18}$$

where:

$$f_{tm} = C(f_{cm})^{2/3} \tag{19}$$

with C varying from 0.095 to 0.185, and the result, f_{tm}, given in $kNcm^{-2}$. It should be noted that Ottosen failure criterion reduces to either Von Mises or Drucker-Prager criteria when $\beta = c_2 = 0$ or $\alpha = c_2 = 0$ are, respectively, assumed. Another aspect considered in this paper is that the concrete in compression has isotropic hardening. When considering zeroed initial yielding stresses, the plastic region, i.e. where the material behaves elastoplastically with hardening, occurs for values of σ_{ef} inside the $0 \le \sigma_{ef} \le f_{cm}$ interval, as illustrated in figure 11. The hardening rule defines the way by which the yielding surfaces move (load surfaces), during plastic deformation. In this paper, a stress-strain curve (figure 12) proposed by the CEB-FIP Model Code 1990 [12] to represent the concrete behavior under uniaxial compression was used. The stress-strain curve is given by:

$$\sigma = -\frac{-\frac{E}{f_{cm}}\varepsilon - \left(\frac{\varepsilon}{-0{,}0022}\right)^2}{1 + \left(\frac{E}{f_{cm}}0{,}0022 - 2\right)\frac{\varepsilon}{-0{,}0022}} f_{cm}, \tag{20}$$

5.3 Constitutive models for concrete in tension

The smeared crack approach was used to model cracked concrete. In this approach, the stress-strain relation is updated after a crack develops, with no modification of the finite element mesh topology during the analysis.
The concrete in tension is modeled as being an elastic material with strain-softening following Ottosen failure criterion. When a material point reaches the failure surface, the failure state in tension or in compression is identified according to the criterion established by the CEB-FIP Model Code 1990 [12] as:

Figure 11 – Loading and failure surfaces

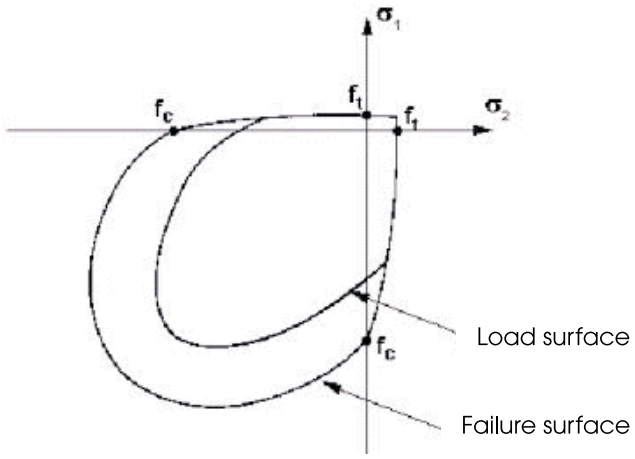

Figure 12 – Stress-strain diagram for the concrete in compression

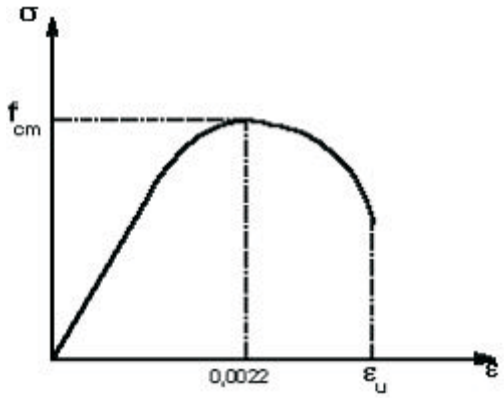

• se $\sigma_1 \geq f_{tm}/2$, the integration point has been cracked;
• se $\sigma_1 < f_{tm}/2$, the integration point has been crushed.

Cracks form on the orthogonal plane to σ_1. After that, it is considered that the concrete is orthotropic with insignificant Poisson effect and local material axes coinciding with the principal stress directions. The crack direction is considered to be fixed, whose approach is known as 'fixed crack approximation'. For a cracked point, a second crack occurrence can be verified, which, for simplicity, is considered orthogonal to the first one. If two cracks occur, the concrete is not supposed to contribute any longer to the structure's strength. The concrete stresses are then zeroed at the point under consideration. The crack direction is calculated solving an eigenvalue problem, i.e. by determining the co-sines of the angles formed between the eigenvalue equivalent to the maximum principal stress, σ_1, and the stress state, which originated the crack.

It is realized that the concrete between cracks resists tension stresses to a certain level, provides bonding to the reinforcement bars and contributes to the total stiffness of the structure. This effect is known as tension stiffening and was incorporated into the model by modifying the stress-strain concrete curve. An exponential curve suggested by Hinton [13], as illustrated in figure 13 is used to simulate the softening effect of strains. This curve is given by:

$$\sigma = E\varepsilon_0(\exp(-(\varepsilon-\varepsilon_0)/\alpha) \quad (21)$$

Figure 13 – Stress-strain curve for the concrete in tension (13)

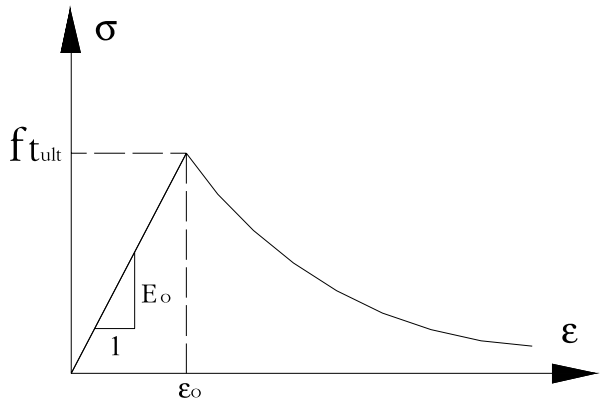

Figure 14 – Stress-strain diagrams: (a) reinforcing steel (b) prestressing steel

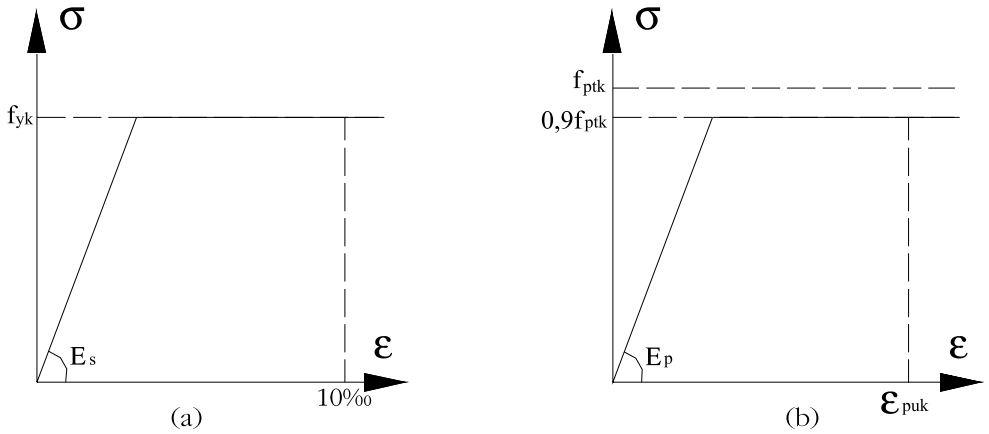

where:
- E is the longitudinal modulus of elasticity;
- ε_0 is the cracking strain;
- α is the softening parameter; and
- ε is the nominal tension strain of the cracked zone.

As a general rule, the first cracks in the concrete under tension are perpendicular to the direction of the higher principal stress, σ_1. The principal directions modify due to changes in loads or because of nonlinearities in the structure, producing relative displacements on the cracks' rough edges and shear stresses on their planes. The values of these shear stresses depend on the local conditions of the cracks. The main transference mechanism of transversal forces is the aggregate interlock, with main variables being the aggregate's type and granulometry.

Additionally, the dowel effect from the reinforcement that crosses the crack is also important to the force transference. The main variables involved in this case are the diameter of the bars, the reinforcement ratio, and the angle of the bars in relation to the crack's plane. Both mechanisms are controlled by crack opening that, when increased, reduces the amount of shear transfer.

These mechanisms cannot be directly included into the smeared crack model and, in fixed crack models, they can be approximated by reducing the value of the concrete transversal modulus of elasticity, G, through a factor β, which varies from 0 to 1 [14]. Thus, the new value for the transversal modulus of elasticity, G_c, is given by:

$$G_c = \beta G \qquad (22)$$

Figure 15 – Evolution of creep strains under constant stress applied

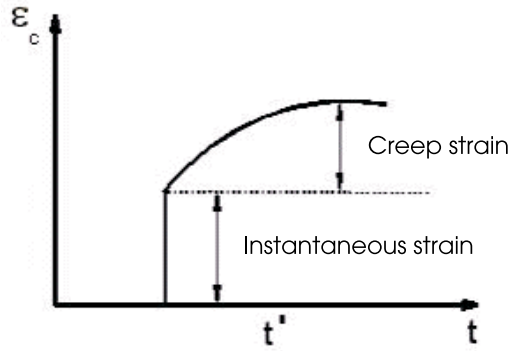

A constant value for β was tried; however, the most realistically approach would be to correlate β with the concrete normal tension strain, ε_t. Cervenka [14] presented the following formula for β, which is also used by Hinton [13], and utilized in this paper:

$$\beta = 1 - (\varepsilon_t / 0{,}005)^{k_1}, \quad (23)$$

where k_1 is taken equal to 0.075.

5.4 Constitutive models for the steel

In structural concrete structures, rebars fundamentally resist axial forces. Therefore, only a uniaxial model to describe their behaviors is necessary. The computational model considers a bilinear stress-strain curve for the steel, i.e. a perfect elastoplastic behavior is considered and its longitudinal modulus of elasticity, E_s, is a parameter of the analysis. For the nontensioned reinforcing steel, an elastic-linear behavior is assumed until the yielding stress value, f_y. For the prestressing steel, an elastic-linear behavior is assumed until 90% of the value of its failure stress, f_{ptk}, is reached according to the CEB-FIP Model Code 1990 [12]. Figures 14a and 14b illustrate the stress-strain diagrams adopted for reinforcing bars and prestressing steel, respectively.

5.5 Viscoelastic models for the concrete and the steel

Time-dependent deformations in concrete are conventionally separated into two types: creep and shrinkage. Creep is the continuous increase in strain that occurs during constant stresses (figure 15). Shrinkage is a reduction in volume of the material in the absence of loads. For prestressed concrete structures the consideration of creep and shrinkage deformations is important because they present a series of undesirable effects such as increase in deflections and prestressing losses. Their values are in the same order of magnitude as of those of instantaneous strains for typical stress levels.

The rheological model adopted to represent the time-dependant behavior of concrete is a chain of Maxwell elements. The chain model is composed of an association in parallel of springs in series with viscous dashpots, as shown in figure 16. This model can be obtained from the basic visco-elastoplastic model if the equivalent yield stresses are set equal to zero for the friction slider elements.

A linear behavior between creep strains and stresses was assumed, since the service stresses should be under $0.4f_{cm}$, where f_{cm} is the mean compressive strength of concrete), which guarantees this linearity (CEB-FIP Model Code 1990, [12]).

The determination of the parameters $E_\mu(t)$ and $\eta_\mu(t)$ of the rheological model, agreeing with the creep function given by the CEB-FIP Model Code 1990 [12], follows the procedure developed by Bazant and Wu [15], and was carried out in Machado [16].

The prestressing steel is subjected to a stress loss due to relaxation. In order to represent this behavior, the same rheological model adopted for the creep effect in the concrete, as shown in figure 16, was used. The same procedure used for the concrete to adjust its rheological parameter was used for the prestressing steel relaxation, as also carried out in Machado[16].

6 Prestressing

Prestressing systems can be classified into three types: pre-tension, post-tension, and external prestressing. In order to address each of these types, three distinct mathematical models were implemented in the program developed and are discussed as follows.

Figure 16 – Maxwell elements chain model for the concrete

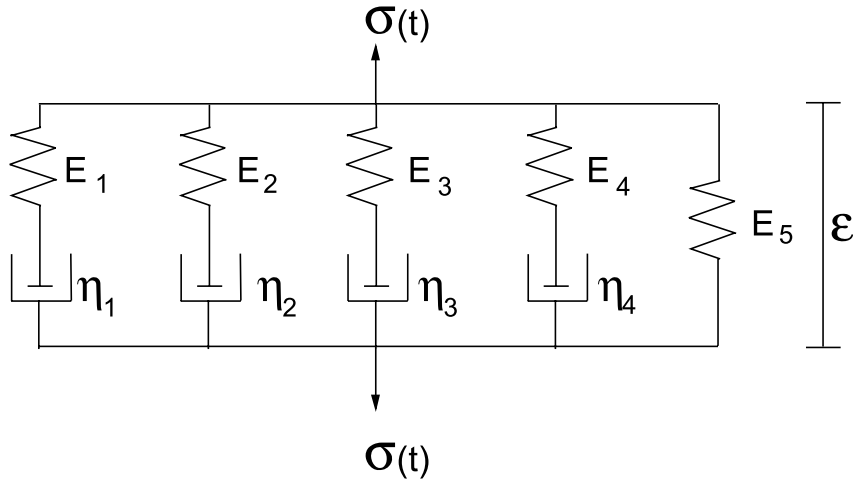

6.1 Pre-tensioned prestressing systems

For the pre-tensioned prestressing system, displacement compatibility is admitted at the point that is shared by the steel and concrete since a perfect bonding hypothesis is assumed between both materials. Another aspect is that both, concrete through creep and shrinkage effects, and the prestressing steel through relaxation, should allow long term strains, which are therefore automatically considered in the computational model and added to immediate stress losses.

6.2 Post-tensioned prestressing systems

In this case the prestressing force is applied on an element of concrete already hardened and the bonding occurs after the injection of grout into the sheaths. The prestressing force is transformed in equivalent nodal forces for the corresponding concrete element, as illustraded in figure 17(a). The axial compressive force, F_p, due to the prestressing tendon is given by:

$$F_p = \sigma_{p0} A_p, \tag{24}$$

where σ_{p0} is the initial prestressing stress (t = 0), at the first integration point (s = 0), and A_p is the cross sectional area of the prestressing steel.

The force, F_p, with components in the global Cartesian directions x and y are:

$$F_{px} = F_p \cos,\alpha$$
$$F_{py} = - F_p \sin\alpha. \tag{25}$$

The equivalent nodal forces, F_{pxi} and F_{pyi}, can be obtained from:

$$\begin{Bmatrix} (F_{px})_i \\ (F_{py})_i \end{Bmatrix} = \sum_{i=1}^{n} \begin{bmatrix} N_i & 0 \\ 0 & N_i \end{bmatrix} \begin{Bmatrix} F_{px} \\ F_{py} \end{Bmatrix}, \tag{26}$$

where N_i is the shape function for the *i*th node of the concrete element.
The prestressing stress loss due to friction can be calculated, according to Vasconcelos [23], by:

$$\sigma_{p0} = \sigma_{pi} \exp[-\mu(\Delta\alpha + 0{,}0001s)], \tag{27}$$

where:
• σ_{p0} is the initial prestressing stress (t = 0), at any point along the tendon;
• $\sigma_{\dot{p}}$ is the prestressing stress applied at the initial end

Figure 17 – (a) representation of the equivalent nodal forces due to the prestressing load; (b) definition of the parameters s and α

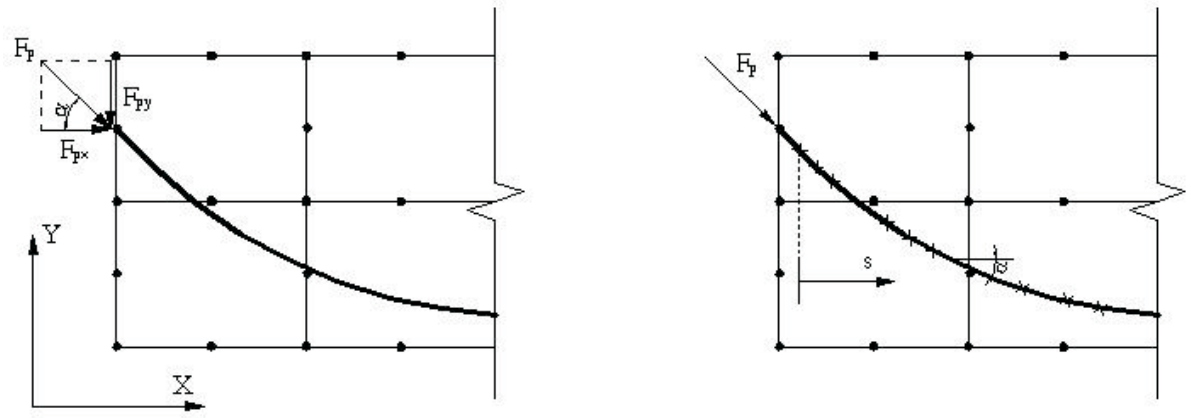

of the tendon (s = 0);
• $\Delta\alpha$ is the total geometric deflection or deviation angle;
• s is the distance between any point along the cable and its initial end;
• μ is the friction coefficient, which is given by:

$$\mu = \begin{cases} 0.50 & \rightarrow \text{direct contact between the steeland the concrete;} \\ 0.30 & \rightarrow \text{direct contact between corrugated steel and metal sheathing;} \\ 0.25 & \rightarrow \text{direct contact between steel and metal sheathing.} \end{cases}$$

The stress variation along tendons is verified at their integration points. The tendon integration point located next to the point where the prestressing load is applied is assumed to be at s = 0. The parameter Δα determines the angle variation between the integration point being considered along the reinforcement in relation to the angle of the point at s = 0 (see figure 17b). For straight tendons, Δα = 0.
Similarly to the pre-tensioned system, progressive losses are automatically considered in the computational model. Increments in stress, total strain, elastic strain, and in plastic strain, as well as the equilibrium of the applied residual forces are calculated and added to the initial stress in the prestressing steel and applied to the external prestressing load.

6.3 External prestressing systems

In external prestressing systems the tendon is free to move along its profile in all sections except at the location of sections at the anchorage and at the deviators. The behavior of the elements with unbonded prestressing subject to bending is complex. It is due to fact that the hypothesis of strain compatibility between concrete and steel is not applicable. Therefore the stress in the tendon depends on the deformation of the entire element, not only on one section. A method that consists of placing the tendon in a dummy mesh was used in order to include the unbonded prestressing tendons in the model. This dummy mesh is parallel to the actual mesh of elements of the structure and only the anchored end nodes and the nodes located at the deviators are common to one another. Therefore there is no strain compatibility between the unbonded tendon and the concrete. For the dummy elements, a low longitudinal modulus of elasticity was adopted, avoiding singularities in the total stiffness matrix.
The absence of adherence only refers to the prestressing tendons while the reinforcing bars are always considered bonded to the concrete and therefore located in the actual mesh of elements.
Figueiras and Póvoas [18] and Moon and Burns [19] state that the main characteristic of externally prestressed structures subjected to bending is that the length variation in the unbonded tendons is equivalent to the total length variation of the structure. Therefore there is compatibility of displacements between the tendons and the structure. This compatibility in displacements, not in strains, in each of the cross sections, allows a practically uniform stress distribution to occur along the unbonded tendon length. This stress distribution is function of the mean concrete strain along the profile of tendons [20].

7 Analysis of an externally prestressed isostatic concrete beam

In this section, the results obtained from the computational model with values determined experimentally by Aparicio *et al.* [6] for one simply supported beam of 7.2 m (24 ft) of effective length will be compared to seven segments and dry joints (figure 18). The CP-190 RB prestressing tendon was composed by four strands of 1.52 cm in diameter (0.60 in.), and is illustrated in figure 18.

Figure 18 – Geometrical characteristics and loading of the beam (6)

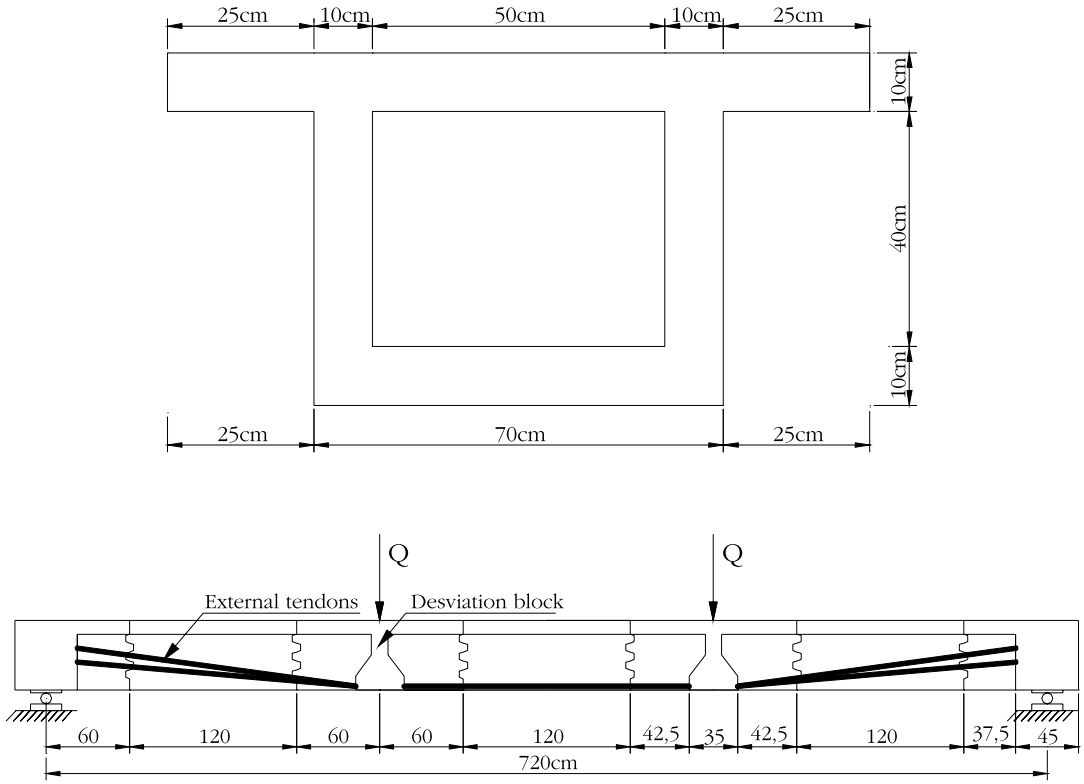

Figure 19 – Discretization of the concrete elements from the left support to the center of the span

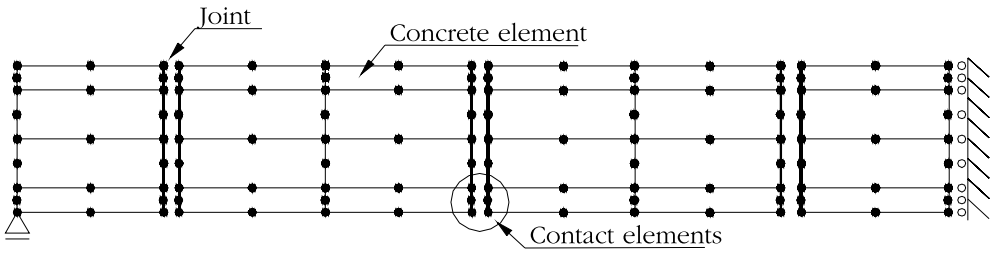

The initial prestressing stress was σ_{p0} = 876 MPa (127 ksi). The steel modulus of elasticity was 195 GPa (28 ksi), and its tensile strength limit, f_{ptk}, was 1900 MPa (276 ksi). The mean compressive strength of the concrete was 45 MPa (6527 psi).

For the finite element analysis, a 24 element mesh was used, with half of the beam discretized due to symmetry conditions in the geometry, properties, and loading, as shown in figure 19. In addition, the size and location of the elements were arranged according to the required thicknesses to model the cross section, i.e., 120 cm for the top flange, 20 cm for the web, and 70 cm for the bottom flange.

Dummy elements, which are parallel to the actual ones, and having in common only the nodes indicated in figure 20, were used to include the unbonded prestressing tendons into the model.

8 Computational model results

In this section, some graphical results obtained with the computational model are presented. The deformed shapes of the beam for different loading levels are shown in figure 21 where, for better visualization, a magnification of 20 x was applied.

Figure 20 – Disposition of the prestressing tendons from the left support to the center of the span

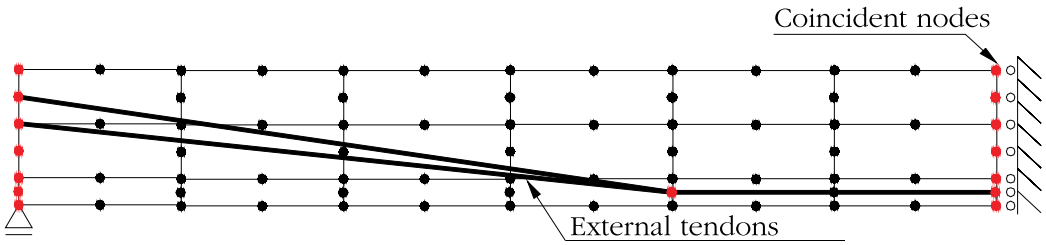

The concrete stress state, in $kNcm^{-2}$, for several levels of applied load is shown in figure 22.
Figure 23a presents curves load (Q) vs. maximum displacement and figure 23b presents curves load (Q) vs. prestressing steel stresses at the midspan cross section of the analyzed beam, according to the computational model and the experimental results.

9 Conclusions

The objective of this paper is to present a model based on the finite element method for a study of the behavior of segmental concrete beams with external prestressing. One beam was analyzed and the results were compared to the experimental data available in the literature. In the service condition, the beam behaved completely compressed and presented a monolithical behavior. This is illustrated in figure 21a and figure 22a. However, when the ultimate state limit is considered, the compressive stresses decreased and tensile stresses appeared, causing the joints to open (figure 21b and 21g). The first joint to open was that one at which the prestressing steel was tilted relatively to the longitudinal axis of the beam. In the graphs of load versus prestressing steel stresses, it can be noticed that due to the joint openings a significant increase in the prestressing steel stresses occurs. As the joints open; the prestressing steel carries the total force in the respective cross sections. The maximum joint opening, for the load of Q = 140 kN, was of 6 mm.
Comparing the results with the available experimental data, it can be verified that the computational simulation of the real behavior of segmentally precast concrete structures is satisfactory, as can be noticed by the agreement between the numerical and the experimental results presented in figure 23. It can be concluded therefore that the finite element method is a valuable tool for the study of precast segmental concrete elements with external prestressing.

10 Acknowledgements

The authors would like to acknowledge the financial support provided for this research by the Coordenação de Aperfeiçoamento de Pessoal de Nível Superior (CAPES) and the Conselho Nacional de Desenvolvimento Científico e Tecnológico (CNPq) in Brazil.

11 References

[01] ROMBACH, G. Precast segmental box girder bridges with external prestressing-design and construction. INSA Rennes Technical University, Hamburg-Harburg, Germany. feb. 2002; 15p.
[02] HINDI, A.; MACGREGOR, R.; KREGER, M. E. & BREEN, J. E. Enhancing strength and ductility of post-tensioned segmental box girder bridges. ACI Structural Journal, v. 92, n. 1, jan-feb. 1995; p. 33-44.
[03] BROCKMANN, C.; ROGENHOFER, H. Bang Na Expressway, Bangkok, Thailand – World´s Longest Bridge and Largest Precasting Operation. PCI Journal, jan-feb. 2000; p. 26-38.
[04] RIBEIRO, A. S. Análise de estruturas compostas por aduelas pré-moldadas de concreto com protensão externa, sob estado plano de tensão, através do Método dos Elementos Finitos, Porto Alegre, 2004, Dissertação de mestrado – PPGEC, Universidade Federal do Rio Grande do Sul, 110p.
[05] HABRAKEN, A. M.; CESCOTTO, S. Contact between deformable solids: The fully coupled approach. Mathl. Comput. Modelling, vol 28, n. 4-8, 1998; p. 153-169.
[06] APARICIO, C. A.; GONZALO, R.; CASAS, R. J. Testing of externally prestressed concrete beams. Engineering Structures, vol 24, n. 4-8, 2002; p. 73-84.
[07] OWEN, D. R. J.; HINTON, E. Finite element in plasticity: theory and practice. Swansea, Pineridge Press, 1980, 594 p.
[08] PANDE, G. N.; OWEN. D. R. J. & ZIENKIEWICZ, O. C. Overlay models in time-dependent non-linear material analysis. Computers and Structures, v. 7, n. 3, 1977; p. 435-443.
[09] ELWI, A. E.; HRUDEY, T. M. Finite element

model for curved embedded reinforcement. Journal of Engineering Mechanics Division, ASCE, vol.115, n.4, 1989, p. 740-745.
[10] ZIENKIEWICZ, O. C. The finite element method. London: McGraw-Hill, vol 1, 4 ed., 1986, 787p.
[11] OTTOSEN, N. S. A failure criterion of concrete. Journal of the Engineering Mechanics Division, ASCE, v. 103, n. 4, aug. 1977; p. 527-535.
[12] COMITÉ EURO-INTERNATIONAL DU BETON. CEB-FIP Model Code 1990. Lausanne, 1993. (Bulletin d'Information, 213/214).
[13] HINTON, E. Numerical methods and software for dynamic analysis of plates and shells. Swansea: Pineridge Press, 1988; 550p.
[14] CERVENKA, V. Constitutive model for cracked reinforced concrete. Journal of the American Concrete Institute, v. 82, n. 6, , 1985; p. 877-882.
[15] BAZANT, Z.P.; Wu, S.T. Rate-type creep law of aging concrete based on Maxwell chain. Matériaux et Constructions, vol.7, n.34, 1974; p. 45-60.
[16] MACHADO, M. S. Aplicação do método dos elementos finitos para a análise elasto viscoplástica de peças de concreto armado e protendido, submetidas a estados planos de tensão, Porto Alegre, 2002, MSc. Thesis in Civil Engineering – Programa de Pós-Graduação em Engenharia Civil, Universidade Federal do Rio Grande do Sul, 150p.
[17] VASCONCELOS, A. C. Manual prático para a correta utilização dos aços no concreto protendido em obediência às normas atualizadas, Rio de Janeiro: Livros técnicos e científicos, editora Ltda, 1980, 64p.
[18] FIGUEIRAS, J. A. & PÓVOAS, R. H. Modelling of Prestress in Non-Linear Analysis of Concrete Structures. Computers & Structures. London, Elsevier Science, v. 53, n. 1, jan. 1994.
[19] MOON, J. & BURNS, N. H. Flexural Behavior of Member with Unbonded Tendons I: Theory. Journal of the Structural Division, New York, ASCE, v. 104, n. 7, jul. 1997.
[20] MATTOCK, A. H.; YAMAZAKI J. & KATTULA, T. Comparative study of prestressed concrete beams, with and without bond. Journal of the American Concrete Institute, v. 68, n. 2, , feb. 1971; p.116-125.

Figure 21 – Deformed shape of the beam according to the computational model

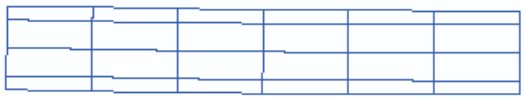

(a) Maximum deflection = - 0.155cm Q=56kN

(b) Maximum deflection = - 0.912cm Q=70kN

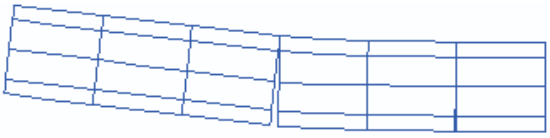

(c) Maximum deflection = - 1.369cm Q=84kN

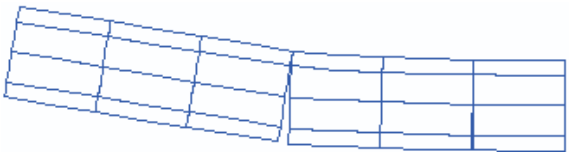

(d) Maximum deflection = - 1,934 cm Q=98kN

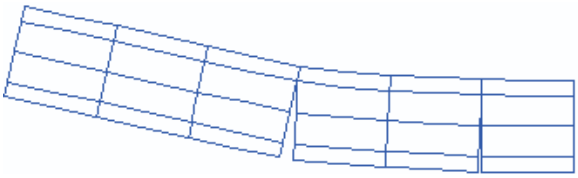

(e) Maximum deflection = - 2,892 cm Q=112kN

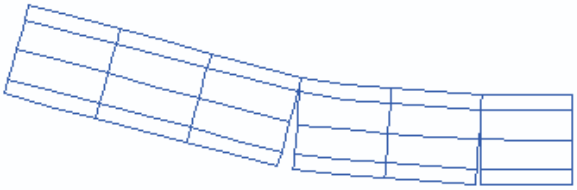

(f) Maximum deflection = - 3.608cm Q=126kN

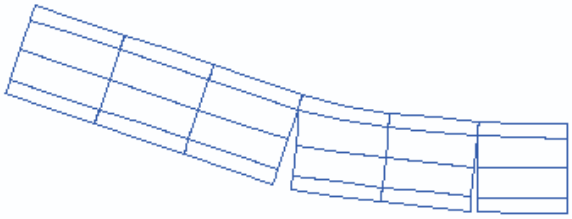

(g) Maximum deflection = - 4.185cm Q=140kN

Figure 22 – Distribution of longitudinal normal stresses in the concrete in kNcm-^{2}

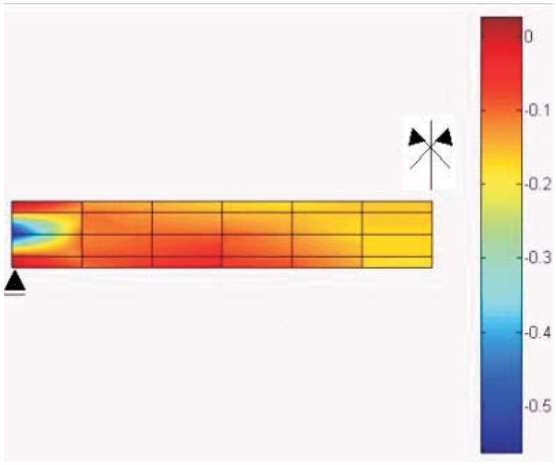

(a) Q=14kN

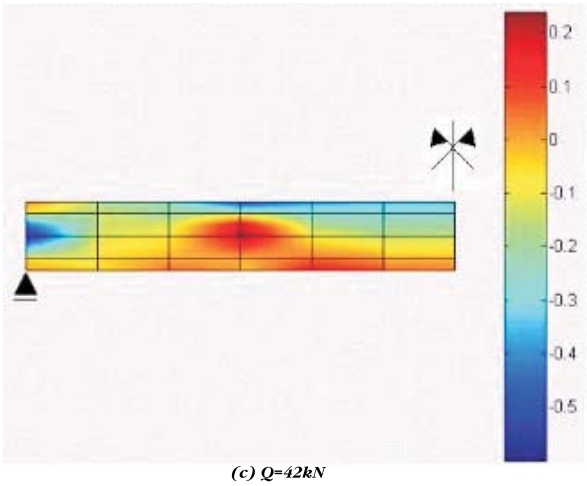

(c) Q=42kN

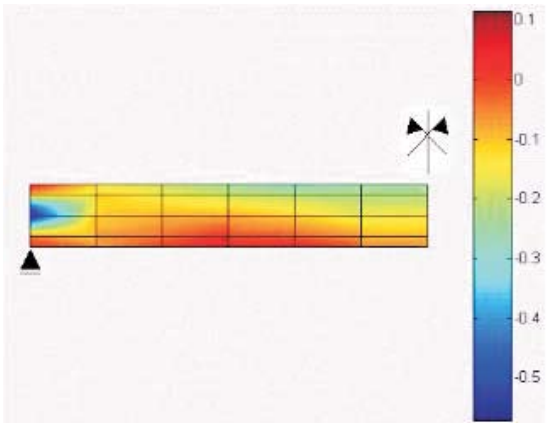

(b) Q=28kN

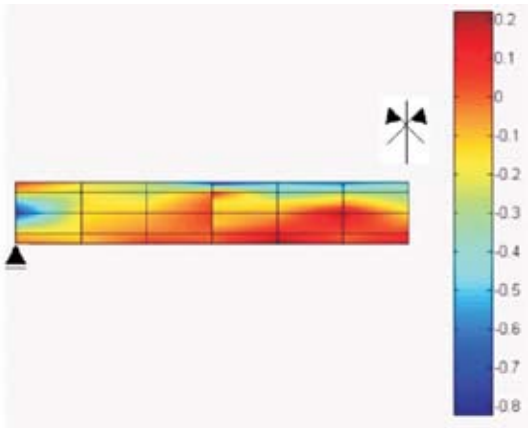

(d) Q=56kN

Figure 22 – Distribution of longitudinal normal stresses in the concrete in kNcm-^{2}

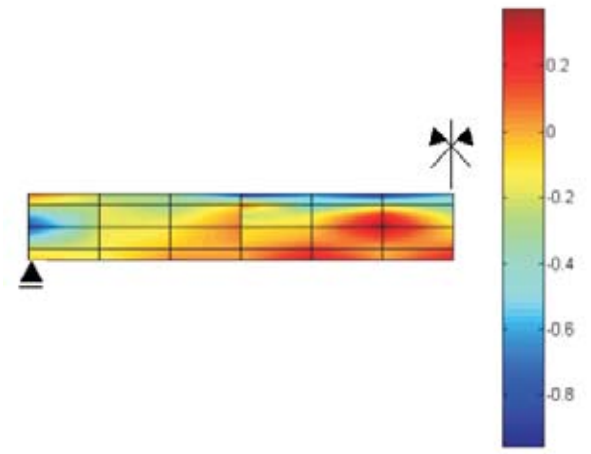

(e) Q=70kN

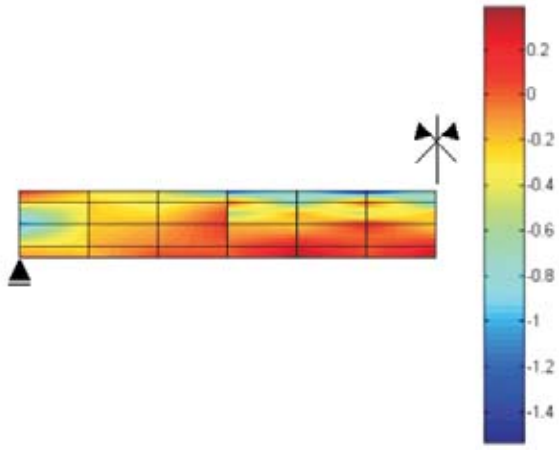

(g) Q=98kN

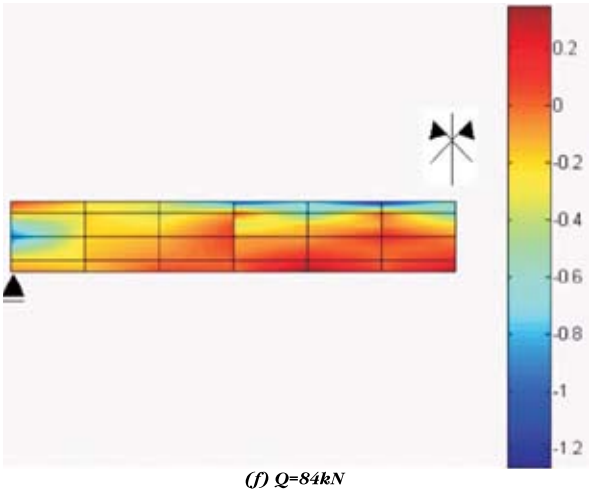

(f) Q=84kN

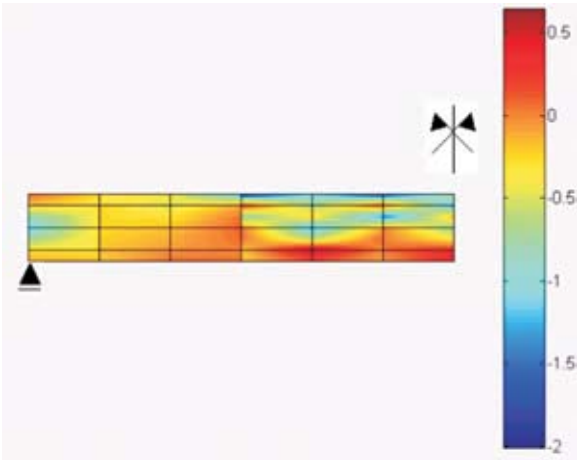

(b) Q=112kN

Figure 22 – Distribution of longitudinal normal stresses in the concrete in kNcm-^{2}

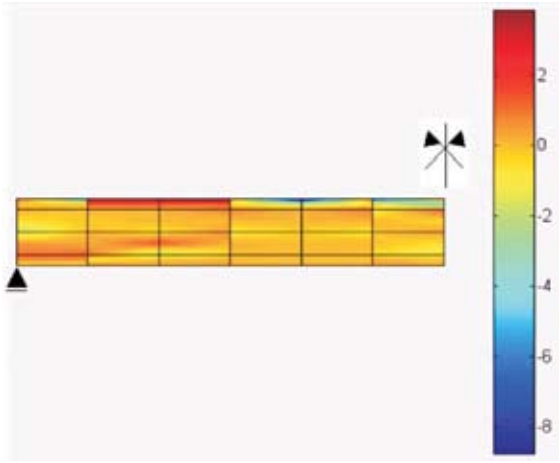

(i) Q=140kN

Figure 23 – Comparison of computational model and experimental results for load versus (a) displacements and (b) reinforcement stresses

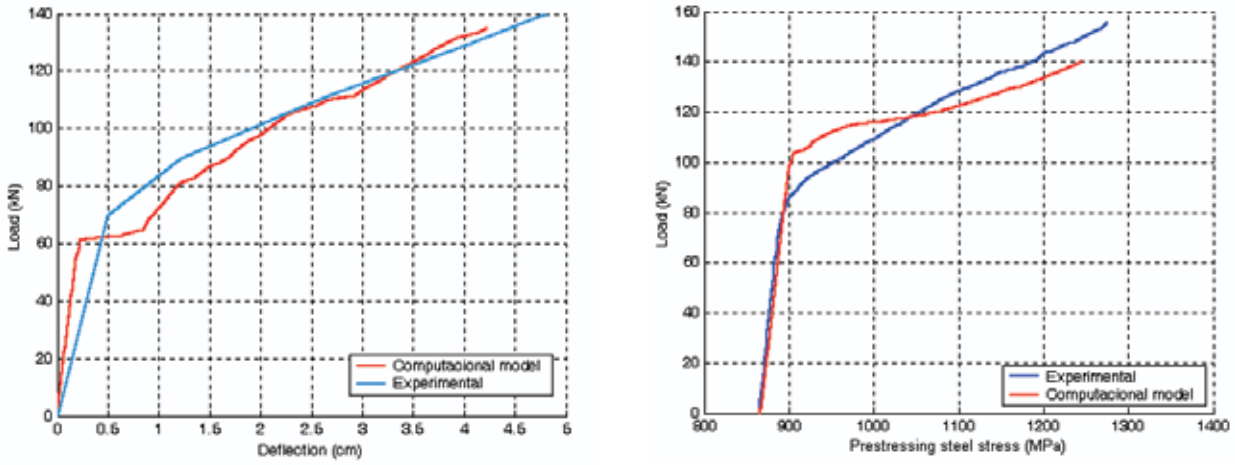

(a) (b)